REPORT
doi:10.26443/seismica.v5i2.3101

SEISMICA

The First Network of Ocean Bottom Seismometers around Jøtul Hydrothermal Vent Field, Knipovich Ridge

Yujie Quan *[1,2], **M.C. Schmidt-Aursch** [1], **Andreia Plaza-Faverola** [3], **V. Schlindwein** [1,2]

[1]Alfred Wegener Institute, Helmholtz Research Centre for Polar and Marine Research, Bremerhaven, Germany, [2]Faculty of Geosciences, University of Bremen, Bremen, Germany, [3]UiT The Arctic University of Norway, Department of Geosciences, Tromsø, Norway

Author contributions: *Conceptualization*: V. Schlindwein, M.C. Schmidt-Aursch. *Data Curation*: M.C. Schmidt-Aursch. *Formal Analysis*: Yujie Quan. *Funding Acquisition*: V. Schlindwein, Andreia Plaza-Faverola. *Investigation*: Yujie Quan. *Resources*: V. Schlindwein, Andreia Plaza-Faverola. *Supervision*: V. Schlindwein, M.C. Schmidt-Aursch, Andreia Plaza-Faverola. *Validation*: Yujie Quan. *Visualization*: Yujie Quan. *Writing – original draft*: Yujie Quan. *Writing – review & editing*: Yujie Quan, M.C. Schmidt-Aursch, V. Schlindwein, Andreia Plaza-Faverola.

Abstract Ultraslow spreading ridges are a vital part of mid-ocean ridge systems, consisting of both magmatic and amagmatic spreading segments. Hydrothermal vents play a key role in the transfer of matter and heat from the lithosphere to the hydrosphere and biosphere. However, research on the relationship between magmatism, faulting, and hydrothermal circulation beneath vent fields on ultraslow spreading ridges is still limited. Here, we investigate Jøtul vent field, situated on a magmatic segment of Knipovich Ridge. We provide continuous passive seismic data recorded by a network of up to 15 broadband ocean bottom seismometers covering up to 50 km along-axis and the time from July 2023 to August 2024. We present our correction for nonlinear clock drift using ambient noise cross-correlation and sensor orientation from Rayleigh wave polarization analysis. Probabilistic power spectral density plots show a clear double-frequency microseismic noise peak. Noise bands at periods of 0.2-0.4 s are likely related to sediment layers and ocean currents. Vibrations of the radio beacon antenna produce noise at periods of 0.16 s. Despite this ambient seismic noise, transient signals of teleseismic, regional, and local earthquakes, and air-gun signals are clearly visible in the dataset enabling studies of seismicity and seismic structure.

Production Editor:
Andrea Llenos
Handling Editor:
Helen Janiszewski
Copy & Layout Editor:
Hannah F. Mark

Received:
May 13, 2026
Accepted:
August 1, 2026
Published:
August 23, 2026

1 Introduction and motivation

Arctic ultra-slow spreading ridges, among the slowest spreading mid-ocean ridge systems on Earth, exhibit distinct characteristics and spreading processes compared to any faster ridge. Ultraslow spreading ridges are composed of linked magmatic and amagmatic accretionary segments (e.g., Dick et al., 2003; Schlindwein and Schmid, 2016). Magmatic segments have thicker oceanic crust and a basaltic seafloor, while little or even no magma is formed in amagmatic segments. Their accretion mode is mainly tectonic, resulting in a thinner or absent crust with mantle rocks exhumed on the seafloor (Jokat et al., 2003; Zhang et al., 2024). The Knipovich Ridge (Fig. 1) is one important part of the Arctic Ridge System, with a full spreading rate of < 15 km/Ma and 35°-50° angle between the spreading direction and the ridge axis trend (Curewitz et al., 2010; Okino et al., 2002). The around 500 km long spreading ridge is bound to the north by the Molloy Fracture Zone and the bend to the Mohns Ridge in the south, featuring a rift valley with depths exceeding 3000 m (Fig. 1). The Knipovich Ridge shows no obvious detachment faults in magma poor spreading zones (Meier et al., 2021). Lateral feeding of melt in volcanic spreading centers along the Knipovich Ridge is limited (Meier et al., 2022), possibly caused by the oblique spreading.

Hydrothermal vent fields are a common geological feature in regions of intense magmatic activity, such as active mantle plume regions, subduction zones, and mid-ocean ridges (Beaulieu et al., 2013). They represent a way to release energy from the Earth's interior and play a key role in material and heat transfer from the lithosphere to the hydrosphere and biosphere. The first hydrothermal system was discovered in the Galápagos rift zone, East Pacific (Rau and Hedges, 1979), and subsequent research revealed numerous hydrothermal vents in other magmatically active zones (Lupton et al., 2006; Vetter and Smith, 2005; Früh-Green et al., 2022). In the 21st century, hydrothermal vent fields have also been discovered along the still poorly explored Arctic Ridge System, e.g. the Aurora vent field (German et al., 2022), Loki's Castle (Pedersen et al., 2010), and the Jøtul vent field (Bohrmann et al., 2024). They provide valuable insight into the diversity and unique characteristics of hydrothermal systems of ultraslow spreading ridges. The Jøtul hydrothermal vent field (Fig. 2) is located in a magmatic spreading segment of northern Knipovich Ridge. This segment is characterized by rough seafloor morphology with a pronounced axial volcanic ridge oriented perpendicular to the spreading direction and elevated fault-bounded blocks forming the rift valley walls. The Jøtul vent field is situated east of the axial volcanic ridge on a potential detachment fault (Bohrmann et al., 2024). Diehl et al. (2026) suggest that this possible detachment fault plays a role in the hydrothermal circula-

*Corresponding author: yujie.quan@awi.de

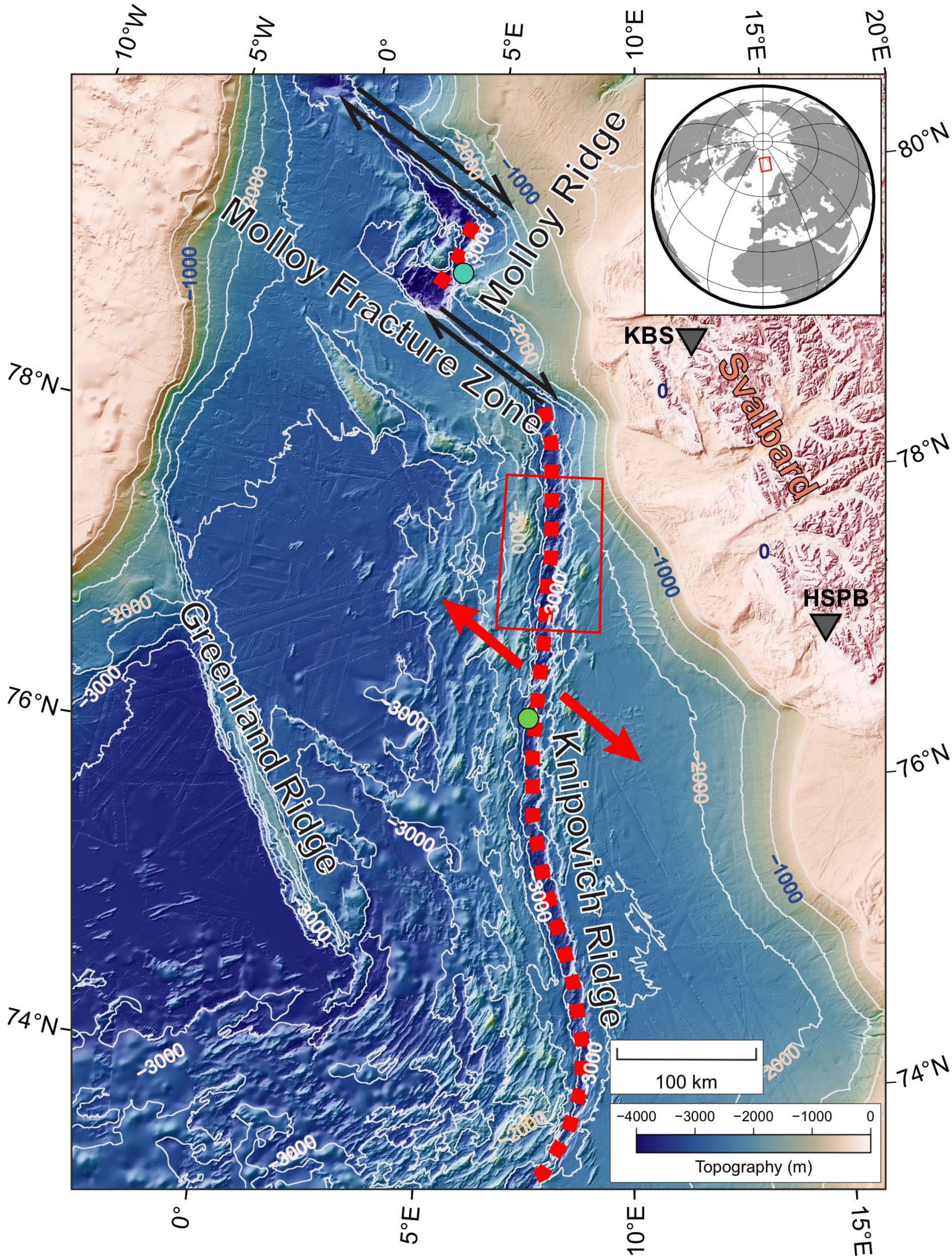

Figure 1 Overview over the topography of the Norwegian-Greenland Sea with the survey area (red box) on Knipovich Ridge. Topography data are from IBCAO version 5.0 (Jakobsson et al., 2024). Circles indicate examples of two regional earthquake epicenters (International Seismological Centre, 2026), which are discussed in section 4.3. Inverse triangles show the land stations used in our experiment. Thick dashed red lines indicate the spreading center and transform faults are plotted by black double arrows. Red arrows show the spreading direction of the Knipovich Ridge. Red box in inset map shows the location of Norwegian-Greenland Sea.

tion of the vent field.

We installed a network of ocean-bottom seismometers (OBSs) centered on Jøtul vent field to investigate hydrothermalism and magmatism on the ultraslow spreading Knipovich Ridge. The data set enables research focusing on the geological structure below seafloor of the northernmost magmatic segment of Knipovich Ridge, the geological setting and functioning of Jøtul vent field, and the relationship between hydrothermalism and magmatism in this magmatic segment.

In this paper, we report the basic processing and the data quality of the seismic network. We show the effects of nonlinear clock drift and document the processing steps and results of the necessary time correction. We provide the orientation angles of the OBS horizontal components. Furthermore, we present an analysis of ambient seismic noise sources and noise levels during deploying period along with examples of transient seismic signals to illustrate the potential of the data set for a variety of research objectives.

2 Instrument deployment and details

2.1 Network geometry and installation

We instrumented the area around Jøtul hydrothermal vent field with a long-term network of 7 OBS stations complemented by a short-term installation of additional 8 stations (Fig. 2, Tab. S1). We deployed stations JOT01-JOT07 in late July 2023 during cruise PS137 of RV Polarstern (Schlindwein, 2023), and added stations JOT08-JOT15 to this network in mid-June 2024 from aboard RV Helmer Hanssen (Plaza-Faverola et al., 2026). All fifteen OBSs were recovered in late August 2024 during cruise MSM131 (Bohrmann et al., 2025). The network was centered on Jøtul vent field, using two roughly circular-shaped observation networks. The diameter of the smaller long-term network was about 20 km until mid-June 2024. It aimed to detect the temporal and spatial earthquake activity around the hydrothermal field and the nearby axial volcanic ridge. The short-term network had larger diameter of about 50 km, to obtain information on the deeper seismic structure of the lithosphere using, for example, ambient noise tomography. Overall, the deepest seismic station of JOT05 was installed at water depth of 3598 m, and the shallowest JOT10 station at a depth of 1965 m below sea level. Stations were deployed in free-fall (velocity: about 0.5 m/s) mode and likewise floated freely (velocity: about 1.0 m/s) to the sea surface upon recovery.

The difference between deployment and recovery location was primarily influenced by wind, waves, and ocean currents acting on the OBS during deployment and recovery. JOT14 experienced the largest drift of 0.77 km distance and a drift angle of 8.29 degree, while JOT01 had the smallest drift distance of 0.10 km distance at an angle of 7.24 degree (for details see Fig. S1 and Tab.S1). However, we should mention that the recovery location is not the specific position where the instrument surfaced, but the location where the instrument was lifted on board. These positions may differ, depending on the amount of time needed to spot the OBS and navigate to its position. Therefore, it will have an influence on the OBS seafloor position. Acoustic ranging of the OBS was not conducted. Operational ship noise of RV Polarstern and RV Helmer Hanssen masks the acoustic response of the OBS beyond about 1000 m water depth. In addition, in a previous experiment with RV Maria S. Merian at a similar mid-ocean ridge location, we received inconclusive acoustic ranging position results, likely because multi-path propagation caused by rough topography is a major challenge for acoustic positioning (e.g., Khan et al., 2026). We therefore estimate the OBS seafloor position to be at 2/3 of the distance between the deployment and recovery position assuming that the 2/3 of the drift occur during the falling of the OBS at half the speed of their rising velocity.

2.2 Instrumentation and recording parameters

Tab. 1 provides an overview of the recording parameters. All instruments apart from JOT07 were K.U.M. Lobster broadband OBS of the DEPAS pool (Deutscher Geräte-Pool für Amphibische Seismologie) (Alfred-Wegener-Institut Helmholtz-Zentrum für Polar- und Meeresforschung et al, 2017a). They consisted of Trillium Compact broadband seismometers with three seismometer channels and a flat instrument response between 0.02 s and 120 s. In addition, a hydrophone channel was recorded getting data from a High-Tech Inc hydrophone. Data were digitized by K.U.M. 6D6 data loggers. The sampling rate for the long-term network of stations JOT01-JOT07 was set to 100 Hz, while that of the short-term network of stations JOT08-JOT15 was 250 Hz. The seismometers were equipped with leveling devices, adjusting a horizontal position upon reaching seafloor with a leveling scheme starting to level the OBS 12 hours after the start of recording and hourly leveling attempts during the subsequent 12 h, followed by daily leveling for a week and subsequently weekly checks of the leveled position. OBS JOT07 was a K.U.M. Nammu OBS equipped with a K.U.M prototype gimballed broadband seismometer, a High-Tech Inc hydrophone, and a K.U.M. 6D7 data logger.

3 Data quality and correction processes

3.1 Instrument performance

All 15 OBSs were recovered successfully, and Fig. 2b and Tab. 1 summarize the state-of-health of all seismometers over the deployment period. The dataset includes about 13 months of data from the long-term deployment, and 2.5 months from the short-term deployment.

Station JOT03 of the long-term network failed for unknown reasons after 58 days of recording (Fig. 2b). The instrument of JOT05 exhausted its battery early, resulting in a record of 308 days from seismometer and hydrophone. During the entire experiment, the vertical channel of JOT07 didn't record any signal. Of the short-term network, which operated for approximately 70 days overlapping with the long-term network,

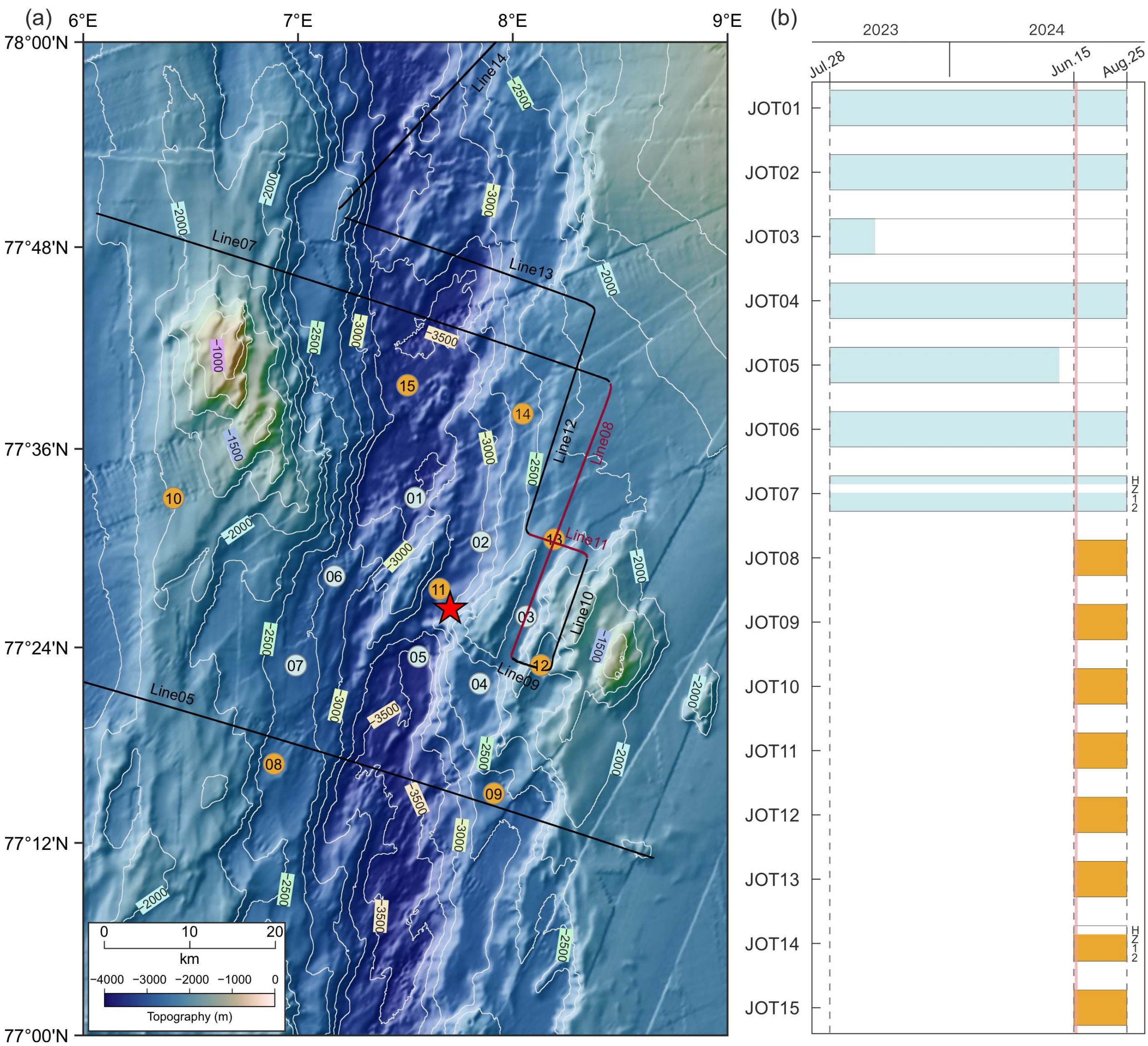

Figure 2 (a) Map of the seismic network around Jøtul hydrothermal vent field (red star). OBSs are marked with circles: blue circles show the long-term deployment, while orange circles indicate the short-term deployment. Nine seismic lines are plotted in red (seismic record sections are shown in supplement) and black (not shown). (b) Data coverage of the stations. Blue and orange areas mean that usable data are collected. Channels are labelled as follows: horizontal channels (1,2), vertical channel (Z), and hydrophone (H). Vertical pink coverage shows the timing of multi-channel seismic survey.

7 instruments recorded data without major anomalies. Only station JOT14 had a damaged hydrophone channel (Fig. 2b). Following the definition of the Cascadia Initiative (Sumy et al., 2015), the ratio of actual volume of recording data to that of data collected if all instruments were normally operating, the data recovery is 83.33% for the seismometer channels, and 85.22% for the hydrophone.

The clock skew is an important parameter for later data processing. Prior to deployment, each OBS clock was synchronized to GPS. Upon recovery, the internal clock was again compared to GPS time, yielding the clock drift or skew. Over the recording period, station JOT06 accumulated a maximum clock drift of -14.232 s, while JOT10 had a minimal skew of -0.103s. The clock of station JOT07 had the lowest average clock drift, with a skew value of only -0.452 s after 393 days of deployment.

3.2 Time correction

Accurate timing is fundamental to many seismic analyses. Timing inaccuracies of OBSs accumulate throughout the deployment period, missing the ability of receiving regularly a GPS signal. Previously, the data were often corrected for a linear clock drift, by applying the measured skew value. However, nonlinear clock drift might occur (Schmidt-Aursch et al., 2026), which can be estimated by ambient noise cross-correlation functions (CCFs) for station pairs (Tian et al., 2021; Hannemann et al., 2013). Here, we do a nonlinear clock drift correction and estimate the necessary correction times based on CCFs calculated with ObsPy (Beyreuther et al., 2010).

Station code	OBSs seafloor location			On date	Off date	SF (Hz)	Duration (days)	Skew (s)	Orientation & error (°)
	Latitude (°)	Longitude (°)	Depth (m)						
JOT01	77.5508	7.5454	3467	2023/07/28	2024/08/23	100	393	-12.856	177±4
JOT02	77.5067	7.5454	3006	2023/07/28	2024/08/23	100	393	-10.317	158±5
JOT03	77.4313	8.0629	2323	2023/07/28	2023/09/23	100	58	-10.475	177±11
JOT04	77.3630	7.8467	2634	2023/07/28	2024/08/24	100	393	-9.513	87±4
JOT05	77.3906	7.5609	3598	2023/07/28	2024/05/31	100	308	-7.639	23±7
JOT06	77.4720	7.1697	2768	2023/07/28	2024/08/25	100	393	-14.232	313±4
JOT07	77.3817	6.9896	2653	2023/07/28	2024/08/25	100	393	-0.452	NaN
JOT08	77.2810	6.8886	2585	2024/06/15	2024/08/25	250	70	-2.663	244±11
JOT09	77.2508	7.9123	2676	2024/06/15	2024/08/24	250	70	-0.496	1±5
JOT10	77.5506	6.4199	1965	2024/06/15	2024/08/25	250	71	-0.103	155±10
JOT11	77.4590	7.6591	3155	2024/06/15	2024/08/24	250	69	-0.858	103±11
JOT12	77.3818	8.1302	2119	2024/06/15	2024/08/24	250	70	-1.382	35±17
JOT13	77.5092	8.1928	2310	2024/06/15	2024/08/23	250	69	-0.210	205±9
JOT14	77.6349	8.0465	2626	2024/06/15	2024/08/23	250	69	-1.094	4±9
JOT15	77.6632	7.510	3456	2024/06/15	2024/08/23	250	69	-1.448	169±9

Table 1 Station parameters for all stations of the Jøtul OBS network. "On date" is the date of deployment, the "off date" is the date of no signal, total power failure, or recovery. Orientation is estimated by the OBS instrument from teleseismic Rayleigh waves (Doran and Laske, 2017).

CCFs can show the relative time shift between a station pair, and the clock drift can be efficiently constrained if a master station communicated regularly with GPS satellites, such as a land station. In our experiment, two onshore stations (KBS: GEOFON Data Centre, 1993; HSPB: Institute of Geophysics, Polish Academy of Sciences, 1990), on the west coast of Svalbard (locations see Fig. 1) were tested as master stations. Before calculating CCFs, we down-sampled all data to 50 Hz to achieve the same sampling frequency for all stations. We then calculated the CCFs from all OBS and land station pairs at daily intervals using the vertical-component. Since the vertical component failed at station JOT07, we used the hydrophone data for JOT07. For clearer CCFs, we tested different cross-correlation parameters. The best results were achieved for a cross-correlation time window of 250 s and a subsequent bandpass filter from 1 to 10 s applied to CCFs of OBS-OBS pairs, and a time window of 350 s and a bandpass filter of 10-100 s for land-station-OBSs pairs, respectively. Unfortunately, the visualization of the CCFs resulting from of OBS-land-station pairs was unsatisfactory for revealing the clock drift, due to the large distance of 170 - 230 km between the OBS networks and the onshore stations (Fig. S2). Therefore, we defined station JOT07 after a linear time correction as our master station because of its minimum skew of -0.45 s after 395 days' deployment (see Tab. 1).

In Fig. 3, we show the time correction result of station JOT06. Time shifts are estimated by calculating the lag time of the peak of another cross-correlation function, obtained from cross-correlating the CCF of each day with that of the first day. CCFs of uncorrected data from the station pair JOT06 and JOT07 indicate a final relative time shift of -13.68 s before clock calibration (Fig. 3a, b), which is consistent with the difference of the skew values between JOT07 (-0.45 s) and JOT06 (-14.23 s). The time shift of the uncorrected data shows a clear deviation with a maximum of about 1 s from an assumed linear clock drift (Fig. 3a). Some black dots in Fig. 3a have visible deviation from the time-shift trend, due to elevated noise levels in the data. In the time correction process, we first do a linear time correction based on the skew. In a second step, we then correct the remaining nonlinear time shift by fitting the observed deviation curve with polynomials of different order (details in Fig. S3) and applying the resulting correction function to shift the seismic traces correspondingly. With the time correction applied, the CCFs between corrected data of stations JOT06 and JOT07 show that the time shift of JOT06 approaches 0 s (Fig. 3a, gray dots) for all days, indicating the effectiveness of our correction procedure. To assess the performance of our correction procedure, we calculated CCFs between all station pairs, and obtained good time correction results for all stations (Figs. S4-S6).

3.3 Correction of OBS orientation

A correct azimuth of the horizontal channel is important for seismic studies using, for example, receiver-functions and ambient noise tomography. Since OBS fall freely to the seafloor, it is difficult to obtain the horizontal channel azimuth without additional analysis. For broadband OBSs, the widely used method is based on teleseismic earthquakes. Here, we apply the orientation correction python package DLOPy (Doran and Laske, 2017), in which seismometer orientation is estimated by Rayleigh-wave polarization analysis (Stachnik et al., 2012). Rayleigh-wave group arrivals of a range frequency windows between 10 and 40 mHz are predicted from a global dispersion model. Grid searching is applied to find the highest cross-correlation coefficient between the vertical component and the Hilbert-

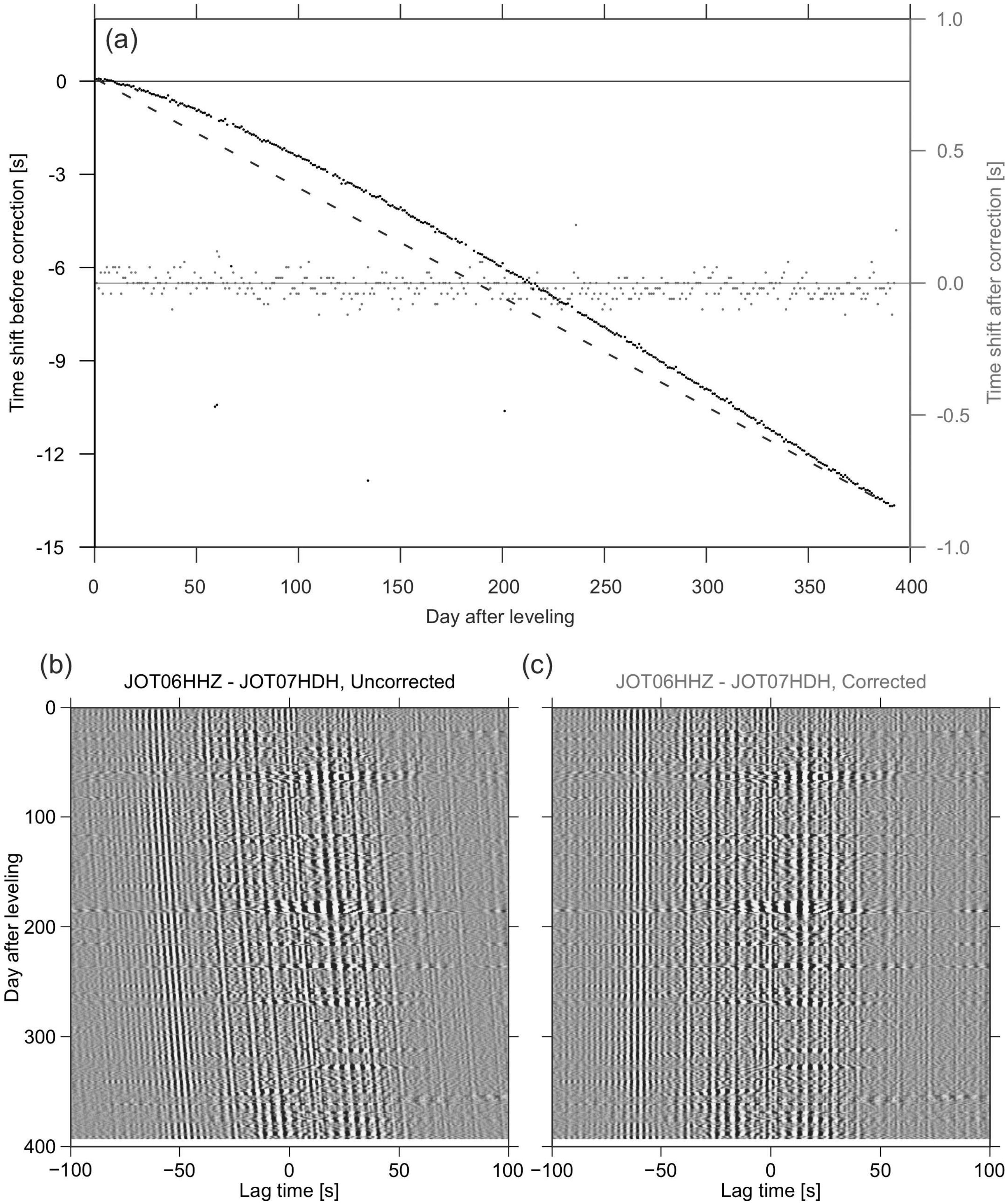

Figure 3 Time correction for station JOT06. (a) Time shifts before and after correction are plotted with black and gray dots, respectively. Dashed line connecting 0 with result of final day, indicates an assumed linear drift. (b) CCFs between the vertical channel of JOT06 (JOT06HHZ) and the hydrophone channel of JOT07 (JOT07HDH) before time correction. (c) CCFs of the JOT06 and JOT07 station pair after time correction. CCFs are filtered between 1 and 10 s.

transformed radial component exploring all possible sensor-event azimuths (Fig. 4b). The orientation (α) is estimated as station-event azimuth (θ) minus sensor-event azimuth (β) (Fig. 4a). The final orientation is estimated as the weight mean of all azimuths whose cross-correlation coefficient exceeds 0.8, while the uncertainty is constrained by the 95% confidence interval of the mean from bootstrapping with 5000 random sam-

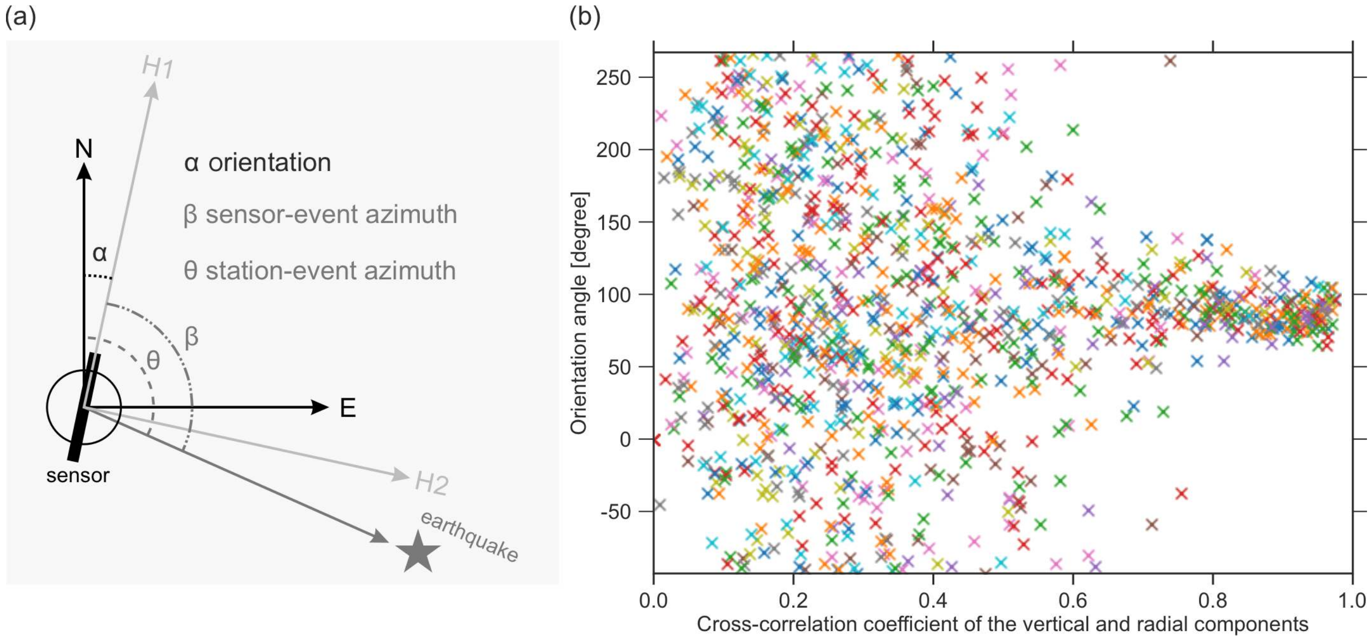

Figure 4 Illustration of the orientation of the coordinate systems and correction result. (a) Relationship of orientation, sensor-event azimuth, and station-event azimuth, modified from Stachnik et al. (2012). (b) Plots of possible orientations and corresponding correlation value using DLOPy, example for JOT04. The crosses are the calculated results of all used teleseismic events with different period filters (at 40 mHz, 35 mHz, 30 mHz, 25 mHz, 20 mHz, 15 mHz, and 10 mHz with a bandwidth of 10 mHz, respectively), plotted with random colour.

ples.

In Tab. 1 and Fig. S7, orientations and their uncertainties are presented for all stations except JOT07 whose vertical channel is damaged. Due to the longer deployment time for JOT01-JOT07, their correction results exhibit a higher stability and have lower uncertainties, compared to those of JOT08-JOT15. We used 135 M_w > 6.0 earthquakes for this analysis, and orientation corrections are estimated with > 100 high-quality measurements on > 25 events for JOT01-JOT06, while > 20 high-quality measurements on > 5 events were used for JOT08-JOT15.

4 Initial observations

4.1 Ambient noise

The ambient noise CCFs used for the time correction demonstrate that high-quality empirical Green's functions can be estimated for periods between 1-10 s for vertical-component station pairs in our OBS network. The analysis of the symmetry of CCF amplitudes between negative and positive lag times can reveal the spatial distribution of microseismic noise sources (Zhang et al., 2023). In our CCFs (Figs. 3 and S8) in the 1-10 s period band, both asymmetry and symmetry characteristics coexist, indicating a complex distribution of secondary microseismic noise sources around the study area. In addition, data of our network could be used for example for ambient noise tomography in the future.

4.2 Noise level

Using the probabilistic power spectral density (PPSD) method (McNamara and Buland, 2004), we perform an analysis of the ambient noise of each station. We calculate the PPSDs of each component for all stations using the ObsPy package (Beyreuther et al., 2010). The continuous signals are cut into 1,800 s time segments with an overlap of 50%. The global new high noise model (NHNM) and low noise model (NLNM) of Peterson (1993) are used as reference for comparison.

In Fig. 5, we display the PPSDs of the deepest station (JOT05), the shallowest station (JOT10), and station (JOT11) which is closest to the Jøtul vent field. None of the PPSDs show an obvious single-frequency microseismic peak in the 10-16 s period band. Instead, a clear double-frequency microseismic maximum peak is located in the period band of 2-3 s, which is lower than that of the NHNM and NLNM (4-5 s). The offset of the locally generated double-frequency microseismic maximum peak (e.g., Bromirski et al., 2005; Schlindwein et al., 2025) may be influenced by the shorter period of ocean waves in the Norwegian-Greenland Sea compared to the global models. The noise power of the vertical channel PPSDs ranges between the NHNM and NLNM. Horizonal channels, however, are 0-50 dB above the NHNM for periods longer than 10 s, caused by the noise of instrument tilt (Crawford and Webb, 2000), and roughly close to the NHNM in the range of the double-frequency microseism (period of 1-10 s). We observe a stronger amplitude in period of 0.2-0.4 s appearing more prominently in the horizontal channel PPSDs, for example, of stations JOT11 CH1 and CH2 and JOT05 HH2, but also to a lesser extent for JOT11 CHZ. The complete PPSD results are shown in Figs. S9-S10.

The spectrograms in Fig. 6 provide an overview of the temporal evolution of the typical noise level recorded by the long-term network, and offer further insights into the data quality. The most prominent signal on

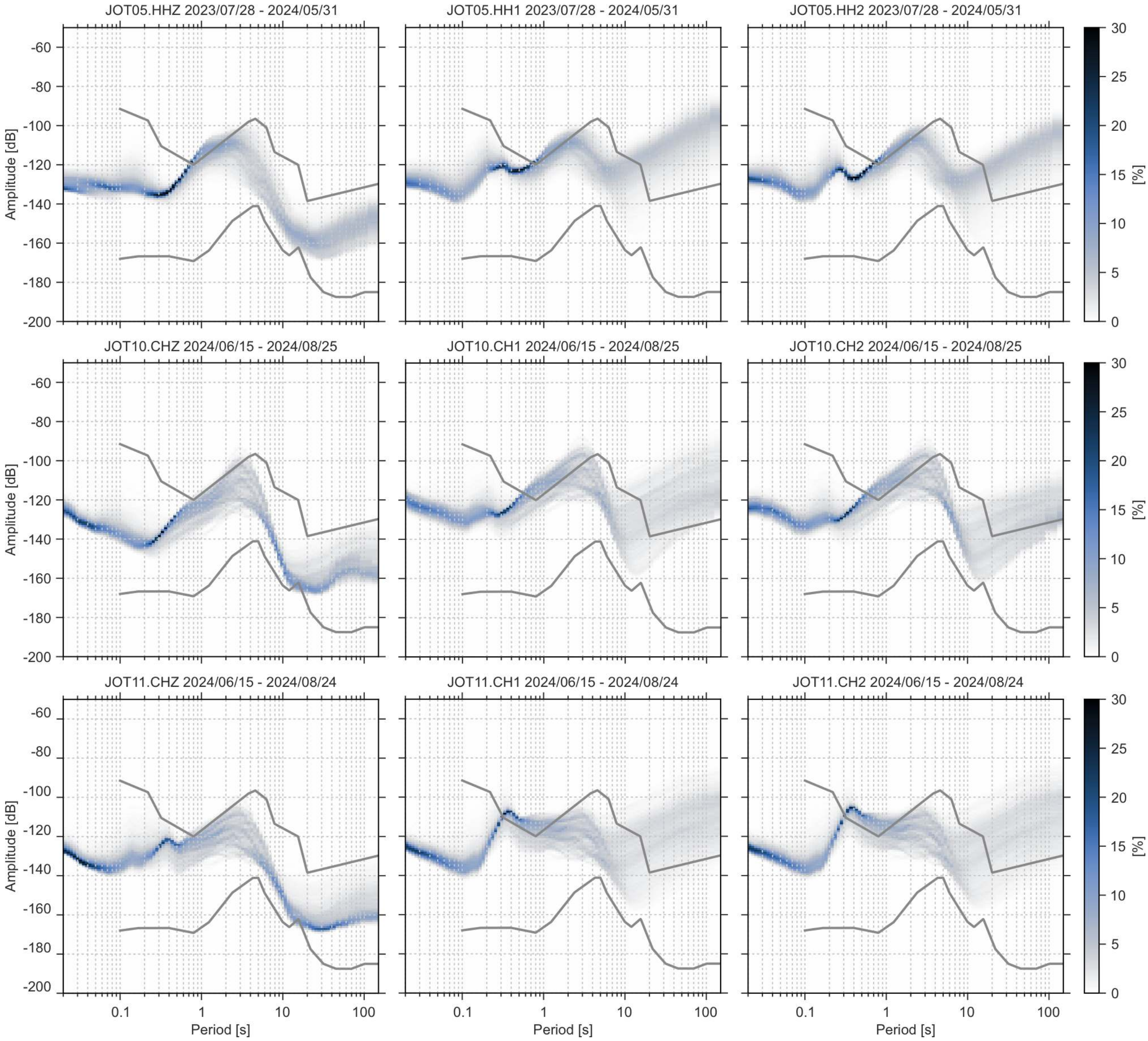

Figure 5 Probabilistic power spectral density (PPSDs) plots of 3 channels (left: vertical component, middle and right: horizontal components) of stations JOT05, JOT10, and JOT11, respectively. The time frame used for calculation is indicated on top of each PPSD plot. Color marks the frequency of occurrence of different noise amplitudes, where gray indicates relatively rare, and dark blue is relatively frequent (McNamara and Buland, 2004). The two gray curves mark the upper and lower bounds of the new high noise model (NHNM) and low noise model (NLNM), respectively (Peterson, 1993).

the channels of all stations is the double-frequency microseism in the range of 0.5-10 s. This signal exhibits strong seasonality with about 20 dB greater amplitude during the winter season from Oct. 2023 to May 2024 (Fig. 6a-6c) and somewhat higher periods of the highest peaks in spectral amplitudes in winter. In August 2024, in contrast, spectrogram results show a time period with relatively weak microseisms (Figs. 6, S11-S14). The seasonality of the microseismic noise and its amplitudes and periods depend on swell and storm events and the related wave heights and periods (e.g., Schlindwein et al., 2025).

Similar to the PPSD results, the OBSs (Figs. 6, S11-S14) show in the power spectrograms strong, continuous but narrow lines of high amplitude in the period band 0.2-0.4 s. The period of these lines varies between stations, e.g. 0.25-0.35 s for JOT11, while about 0.25 s for JOT02 (Fig. 6b and 6e). It is present on vertical and horizontal channels but not on the hydrophone channel. The likely reason is a distortion of wave fields from irregular boundaries at the sediment rock interface and complicated reflections and conversions in the sediment layer (Atakan and Havskov, 1996; Prothero, 1984). At about 0.16 s (6 Hz), a prominent intermittent signal appears in the power spectrograms (Fig. 6a and 6b), which is likely caused by ocean current induced vibrations of the radio beacon antenna on the OBS (Essing et al., 2021).

Several hydrophones didn't work well during deployment, exhibiting straight lines without variation in PPSDs and unusual low noise in spectrograms (Figs. 6c, S9-S11 and S13), such as 2 months after deploying for JOT02 and during entire deployment for JOT10. We

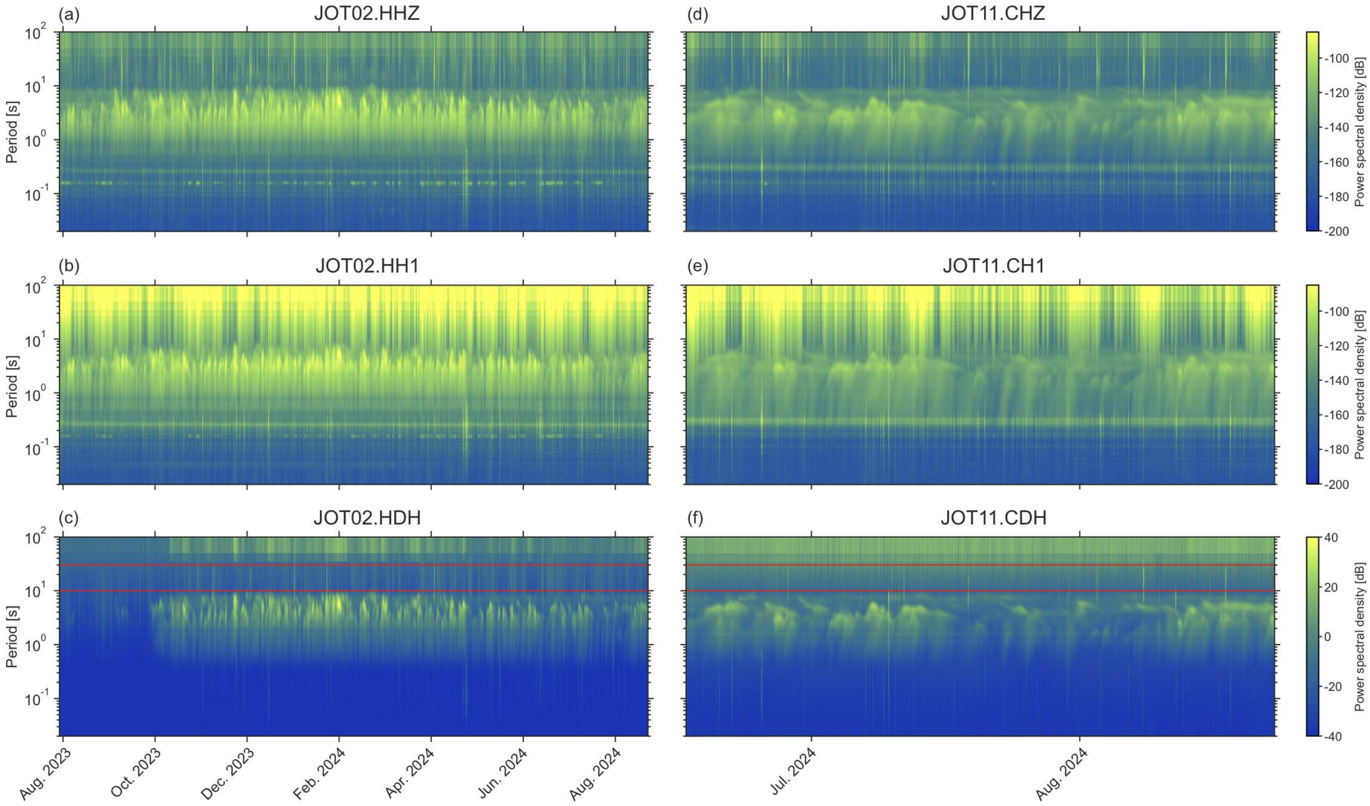

Figure 6 Power spectrograms from stations JOT02 (a, b, c) and JOT11(d, e, f) for the vertical (a, d), the first horizontal (b, e) and the hydrophone channel (c, f), respectively. The double-frequency microseism, a band of high spectral power between 0.5 and 10 s, is visible on both stations. Red lines on the hydrophone channel spectrograms indicate the range of the 10-30 s noise notch.

also observe the so-called noise notch at 10-30 s during the entire deployment (Fig. 6c and 6f), which is a common phenomenon of seismic records in the global oceans (Webb, 1998). This is shown more obviously on the hydrophone channel since the seismometers suffer from high noise at long periods, which is caused by a higher sensitivity to instrument tilt (Crawford and Webb, 2000; Webb, 1998). Therefore, there is no major noise source in this period band in our study area, and the noise notch provides a high signal-noise-ratio window for studying seismic signals.

4.3 Transient earthquake signals of OBSs

We conduct a qualitative assessment of waveform quality for earthquakes from different epicentral distances. As an example of a teleseismic earthquake, we display the waveform of a strong earthquake from Honshu, Japan, with magnitude Ms= 7.2, filtered between 20 and 100 s (Fig. 7a). The P and S phases are obvious on the channels of station JOT05, as well as the clear, dispersive surface wave later on.

Waveforms of regional earthquakes (event 1 from Molloy Ridge with Ms=3.4, event 2 from 76.4 °N on Knipovich Ridge with Ms=4.3, for locations see Fig. 1) filtered with a 1-5 Hz bandpass filter show visible T-phases after the P and S seismic waveforms (Fig. 7b). The T-phase is generated by seismic-acoustic conversion and travels along the minimum sound velocity layer in the ocean (e.g., Okal, 2008). Regardless of whether the event occurs outside the network to the north or south, the T-phase of the deepest station JOT05 exhibits the relatively smallest amplitude, indicating that the T-phase amplitude may be influenced by seafloor topography and water depth of the instrument.

Fig. 7c shows the waveforms and manual phase picks used for preliminary location (77.722 °N, 7.602 °E) of a local event which occurred just to the north of the network. It exhibits clear P and S phases on vertical (and horizontal) channels of different stations, after filtering between 3 and 15 Hz. This local event is well recorded across the entire network from north (earliest arrival at JOT15) to south (last arrival at JOT09) with most stations showing a clear signal of the P and S phases on the vertical (and horizontal) channel.

Therefore, the dataset of our network has a significant value for seismic waveform analysis of any kind. It can be used for a variety of seismic imaging methods to probe the oceanic crust and mantle structure, such as receiver functions and body-wave tomography. Moreover, these data can provide new unique ray paths to help constrain global and regional models of seismic structure under the Knipovich Ridge.

4.4 Seismic signals of air-gun profiling

During the short-term deployment, some multichannel seismic survey lines were acquired (Fig. 2) from June 16 to June 17, 2024 around our networks (Plaza-Faverola et al., 2026). The seismic source consisted of two GI (generator/injector) air-guns with a volume of 30 in3 (G 15 / I 15). The air-guns were towed

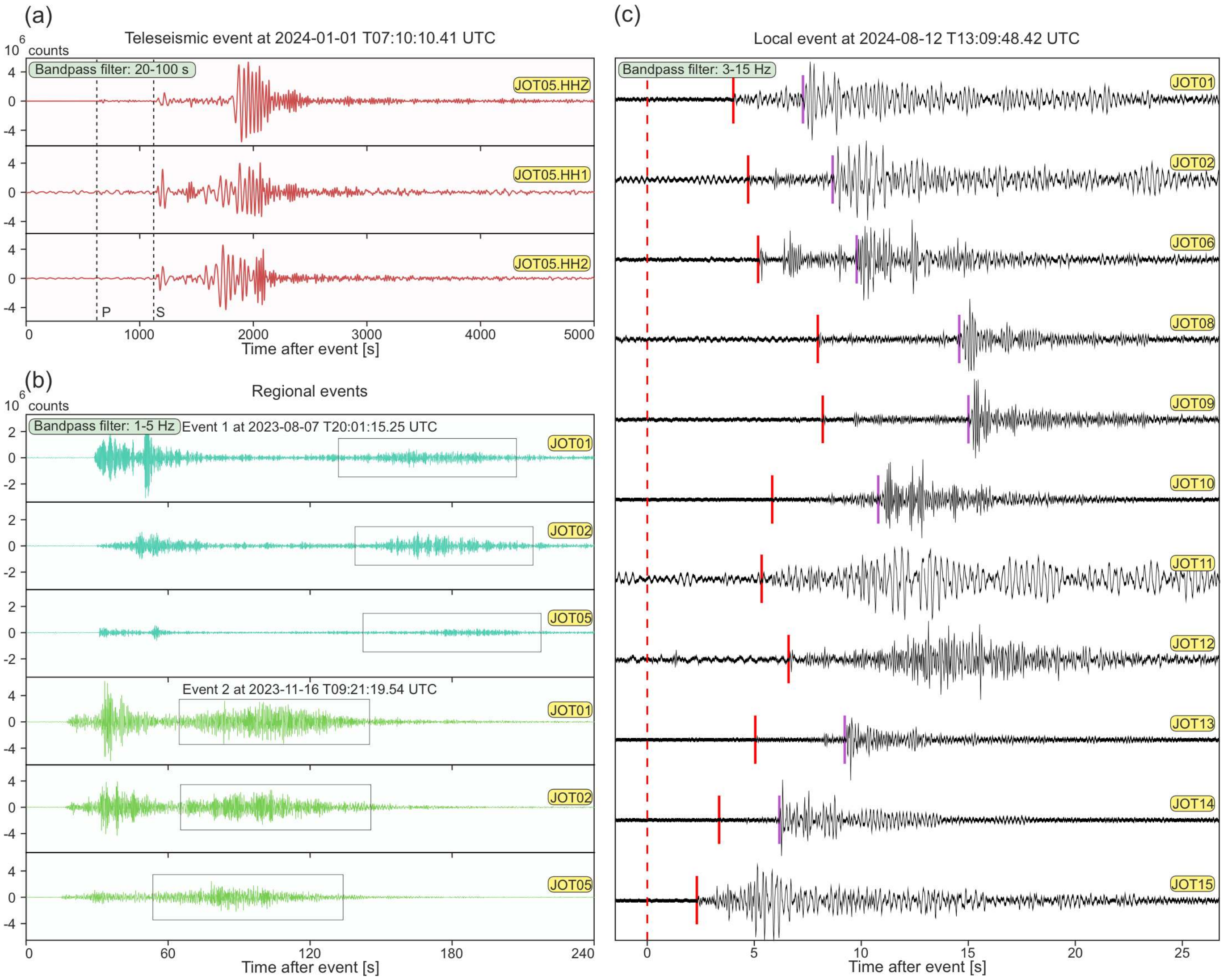

Figure 7 Signal examples of teleseismic, regional, and local events. (a) Signal waveform of earthquake with Ms=7.2 from the west coast of eastern Honshu after bandpass filter of 20-200 s. (b) 1-5 Hz bandpass filtered signal of raw vertical channels from two regional seismic events (locations see in Fig. 1), possible T-phases are enclosed in the black boxes. (c) A vertical-channel array gather of a local earthquake, with a hypocentre outside the network, filtered between 3 and 15 Hz. Amplitudes are normalized by the absolute maximum value of each trace. Markers are manual P (red) and S (purple) picks.

at a speed of 4-5 knots, firing once every 6-7 s. These active seismic signals of 50-300 Hz were also received by our OBSs.

The example of record sections of air-gun signals in Fig. S15 exhibits clear direct water wave phase (Pw), refracted wave phase from sediment layers or crust (Pg), reflection wave from sediments or basement (Pr). The named phases only can be observable at short offsets, due to the relatively low power of the seismic source and the short shot interval of 6 s as opposed to typical shot intervals used in seismic wide-angle surveys.

5 Summary

From June 2023 to August 2024, we installed a long-term network and a short-term seismic network, centered on Jøtul hydrothermal vent, and successfully recovered the 15 DEPAS broadband ocean bottom seismometers. The overall performance of the network was very satisfactory, but some issues, such as damages on hydrophones and seismometers and exhausted batteries, impact the data return of our experiment.

We applied a clock time correction using ambient noise cross-correlation functions, and retrieved sufficiently accurate seismometer orientation angles from teleseismic earthquakes except for station JOT07.

Noise level analysis indicates high signal-noise ratio for seismic signals. Noise with periods of 0.2-0.4s existed during the entire deployment, which can hopefully be used to advance the understanding of structure of sediment layers in the study area. Double-frequency microseismic noise exhibits a strong seasonality. Transient seismic signals of teleseismic, regional, and local earthquakes and multi-channel seismic surveying can clearly be identified in the data set enabling a variety of seismic studies.

Acknowledgements

We would like to acknowledge the crew and scientists of cruises PS137, MS131, and UiT-IG24-7. We thank the "German Instrument Pool for Amphibian Seismology (DEPAS)", hosted by the Alfred Wegener Institute Bremerhaven, for providing the ocean-bottom seismometers. Shiptime on RV Polarstern (Alfred-Wegener-Institut Helmholtz-Zentrum für Polar- und Meeresforschung et al, 2017b) cruise PS137 was granted under AWI_PS137_02. Yujie Quan is financially supported by China Scholarship Council (CSC, 202404910114). Constructive comments by two anonymous reviewers and Editor Helen Janiszewski improved the quality of our work. The data is processed and visualized using software of ObsPy (Beyreuther et al., 2010), GMT (Wessel et al., 2019), and Seismic Unix (Cohen and Stockwell, 2008).

Data and code availability

The data of the onshore stations can be retrieved from the GEOFON data base (KBS: GEOFON Data Centre, 1993; HSPB: Institute of Geophysics, Polish Academy of Sciences, 1990). The time-corrected OBS data have been submitted to GEOFON. The OBS raw data are available in the PANGAEA repository (Schlindwein et al., 2026).

Competing interests

The authors declare no competing interests to this study.

References

Alfred-Wegener-Institut Helmholtz-Zentrum für Polar- und Meeresforschung et al. DEPAS (Deutscher Geräte-Pool für amphibische Seismologie): German Instrument Pool for Amphibian Seismology. *Journal of large-scale research facilities JLSRF*, 3:A122, Nov. 2017a. doi: 10.17815/jlsrf-3-165.

Alfred-Wegener-Institut Helmholtz-Zentrum für Polar- und Meeresforschung et al. Polar Research and Supply Vessel POLARSTERN Operated by the Alfred-Wegener-Institute. *Journal of large-scale research facilities JLSRF*, 3:A119, Oct. 2017b. doi: 10.17815/jlsrf-3-163.

Atakan, K. and Havskov, L. Local site effects in the northern North Sea based on single-station spectral ratios of OBS recordings. *Terra Nova*, 8(1):22–33, Jan. 1996. doi: 10.1111/j.1365-3121.1996.tb00722.x.

Beaulieu, S. E., Baker, E. T., German, C. R., and Maffei, A. An authoritative global database for active submarine hydrothermal vent fields. *Geochemistry, Geophysics, Geosystems*, 14(11):4892–4905, Nov. 2013. doi: 10.1002/2013gc004998.

Beyreuther, M., Barsch, R., Krischer, L., Megies, T., Behr, Y., and Wassermann, J. ObsPy: A Python Toolbox for Seismology. *Seismological Research Letters*, 81(3):530–533, May 2010. doi: 10.1785/gssrl.81.3.530.

Bohrmann, G., Streuff, K., Römer, M., Knutsen, S.-M., Smrzka, D., Kleint, J., Röhler, A., Pape, T., Sandstå, N. R., Kleint, C., Hansen, C., dos Santos Ferreira, C., Walter, M., de Paula Santos, G. M., and Bach, W. Discovery of the first hydrothermal field along the 500-km-long Knipovich Ridge offshore Svalbard (the Jøtul field). *Scientific Reports*, 14(1), May 2024. doi: 10.1038/s41598-024-60802-3.

Bohrmann, G., Anagnostou, E., Asatrian, K., Barrenechea Angeles, I., Bergenthal, M., Berger, F., Büttner, H., Diehl, A., Feddersen, G., Franke, R., Jain, A., Kienitz, T., Knutsen, S. M., Kopiske, E., Malnati, J., Marcon, Y., Meckel, E.-M., Meyer, M., Pilot, M., Rehage, R., Reuter, C., Ribeiro, P., Röhler, A., Römer, M., Schillai, S., Schlindwein, V., Schröder, M., Spiesecke, U., Streuff, K., Strmic-Palinkas, S., and Von Wahl, T. The Jøtul hydrothermal field - Magma-sediment interaction at the ultraslow-spreading Knipovich Ridge, Cruise No. MSM131, 18 August - 28 September 2024, Reykjavik (Iceland) - Emden (Germany), 2025. doi: 10.48433/CR_MSM131.

Bromirski, P. D., Duennebier, F. K., and Stephen, R. A. Mid-ocean microseisms. *Geochemistry, Geophysics, Geosystems*, 6(4), Apr. 2005. doi: 10.1029/2004gc000768.

Cohen, J. and Stockwell, J. *CWP/SU: Seismic Un*x Release No. 43: an open source software package for seismic research and processing Center for Wave Phenomena*. Colorado School of Mines, 2008.

Crawford, W. and Webb, S. Identifying and Removing Tilt Noise from Low-Frequency (<0.1 Hz) Seafloor Vertical Seismic Data. *Bulletin of the Seismological Society of America*, 90(4):952–963, Aug. 2000. doi: 10.1785/0119990121.

Curewitz, D., Okino, K., Asada, M., Baranov, B., Gusev, E., and Tamaki, K. Structural analysis of fault populations along the oblique, ultra-slow spreading Knipovich Ridge, North Atlantic Ocean, 74°30′N-77°50′N. *Journal of Structural Geology*, 32(6), 2010. doi: 10.1016/j.jsg.2009.08.011.

Dick, H. J. B., Lin, J., and Schouten, H. An ultraslow-spreading class of ocean ridge. *Nature*, 426(6965):405–412, Nov. 2003. doi: 10.1038/nature02128.

Diehl, A., Anagnostou, E., Monien, P., Pape, T., Meckel, E.-M., Römer, M., Mezri, L., Bach, W., Monien, D., Hansen, C., Röhler, A., Streuff, K., Palinkas, S. S., Marcon, Y., Barrenechea Angeles, I., Kleint, C., Knutsen, S., and Bohrmann, G. High H2 production in sediment-hosted hydrothermal fluids at an ultraslow spreading mid-ocean ridge. *Communications Earth & Environment*, 7 (1), Jan. 2026. doi: 10.1038/s43247-025-02962-2.

Doran, A. K. and Laske, G. Ocean-Bottom Seismometer Instrument Orientations via Automated Rayleigh-Wave Arrival-Angle Measurements. *Bulletin of the Seismological Society of America*, 107 (2):691–708, Jan. 2017. doi: 10.1785/0120160165.

Essing, D., Schlindwein, V., Schmidt-Aursch, M. C., Hadziioannou, C., and Stähler, S. C. Characteristics of Current-Induced Harmonic Tremor Signals in Ocean-Bottom Seismometer Records. *Seismological Research Letters*, 92(5):3100–3112, Apr. 2021. doi: 10.1785/0220200397.

Früh-Green, G. L., Kelley, D. S., Lilley, M. D., Cannat, M., Chavagnac, V., and Baross, J. A. Diversity of magmatism, hydrothermal processes and microbial interactions at mid-ocean ridges. *Nature Reviews Earth & Environment*, 3(12):852–871, Nov. 2022. doi: 10.1038/s43017-022-00364-y.

GEOFON Data Centre. GEOFON Seismic Network, 1993. doi: 10.14470/TR560404.

German, C. R., Reeves, E. P., Türke, A., Diehl, A., Albers, E., Bach, W., Purser, A., Ramalho, S. P., Suman, S., Mertens, C., Walter, M., Ramirez-Llodra, E., Schlindwein, V., Bünz, S., and Boetius, A. Volcanically hosted venting with indications of ultramafic influence at Aurora hydrothermal field on Gakkel Ridge. *Nature Communications*, 13(1), Oct. 2022. doi: 10.1038/s41467-022-34014-0.

Hannemann, K., Krüger, F., and Dahm, T. Measuring of clock drift rates and static time offsets of ocean bottom stations by means of ambient noise. *Geophysical Journal International*, 196(2): 1034–1042, Nov. 2013. doi: 10.1093/gji/ggt434.

Institute of Geophysics, Polish Academy of Sciences. Polish Seismological Network, 1990. doi: 10.7914/90RH-0Q80.

International Seismological Centre. ISC Bulletin [dataset], 2026. doi: 10.31905/d808b830.

Jakobsson, M., Mohammad, R., Karlsson, M., Salas-Romero, S., Vacek, F., Heinze, F., Bringensparr, C., Castro, C. F., Johnson, P., Kinney, J., Cardigos, S., Bogonko, M., Accettella, D., Amblas, D., An, L., Bohan, A., Brandt, A., Bünz, S., Canals, M., Casamor, J. L., Coakley, B., Cornish, N., Danielson, S., Demarte, M., Di Franco, D., Dickson, M.-L., Dorschel, B., Dowdeswell, J. A., Dreutter, S., Fremand, A. C., Hall, J. K., Hally, B., Holland, D., Hong, J. K., Ivaldi, R., Knutz, P. C., Krawczyk, D. W., Kristofferson, Y., Lastras, G., Leck, C., Lucchi, R. G., Masetti, G., Morlighem, M., Muchowski, J., Nielsen, T., Noormets, R., Plaza-Faverola, A., Prescott, M. M., Purser, A., Rasmussen, T. L., Rebesco, M., Rignot, E., Rysgaard, S., Silyakova, A., Snoeijs-Leijonmalm, P., Sørensen, A., Straneo, F., Sutherland, D. A., Tate, A. J., Travaglini, P., Trenholm, N., van Wijk, E., Wallace, L., Willis, J. K., Wood, M., Zimmermann, M., Zinglersen, K. B., and Mayer, L. The International Bathymetric Chart of the Arctic Ocean Version 5.0. *Scientific Data*, 11(1), Dec. 2024. doi: 10.1038/s41597-024-04278-w.

Jokat, W., Ritzmann, O., Schmidt-Aursch, M. C., Drachev, S., Gauger, S., and Snow, J. Geophysical evidence for reduced melt production on the Arctic ultraslow Gakkel mid-ocean ridge. *Nature*, 423(6943), 2003. doi: 10.1038/nature01706.

Khan, Z. U., Muhammad, A., Khan, J., Khan, S. U., Abbasi, I. A., Chaudhry, H. N., Alturki, N., and Alanazi, S. Advances in localization techniques and algorithms for UWSNs: A comprehensive review of challenges, opportunities, future directions, and comparative analysis. *Alexandria Engineering Journal*, 137:468–504, Feb. 2026. doi: 10.1016/j.aej.2026.01.039.

Lupton, J., Butterfield, D., Lilley, M., Evans, L., Nakamura, K., Chadwick, W., Resing, J., Embley, R., Olson, E., Proskurowski, G., Baker, E., de Ronde, C., Roe, K., Greene, R., Lebon, G., and Young, C. Submarine venting of liquid carbon dioxide on a Mariana Arc volcano. *Geochemistry, Geophysics, Geosystems*, 7(8), Aug. 2006. doi: 10.1029/2005gc001152.

McNamara, D. and Buland, R. Ambient Noise Levels in the Continental United States. *Bulletin of the Seismological Society of America*, 94(4):1517–1527, Aug. 2004. doi: 10.1785/012003001.

Meier, M., Schlindwein, V., Scholz, J., Geils, J., Schmidt-Aursch, M. C., Krüger, F., Czuba, W., and Janik, T. Segment-Scale Seismicity of the Ultraslow Spreading Knipovich Ridge. *Geochemistry, Geophysics, Geosystems*, 22(2), Feb. 2021. doi: 10.1029/2020gc009375.

Meier, M., Schlindwein, V., and Schmid, F. Magmatic Activity and Dynamics of Melt Supply of Volcanic Centers of Ultraslow Spreading Ridges: Hints From Local Earthquake Tomography at the Knipovich Ridge. *Geochemistry, Geophysics, Geosystems*, 23 (10), Oct. 2022. doi: 10.1029/2021gc010210.

Okal, E. A. *The generation of T waves by earthquakes*, page 1–65. Elsevier, 2008. doi: 10.1016/s0065-2687(07)49001-x.

Okino, K., Curewitz, D., Asada, M., Tamaki, K., Vogt, P., and Crane, K. Preliminary analysis of the Knipovich Ridge segmentation: influence of focused magmatism and ridge obliquity on an ultraslow spreading system. *Earth and Planetary Science Letters*, 202(2), 2002. doi: 10.1016/s0012-821x(02)00790-2.

Pedersen, R. B., Rapp, H. T., Thorseth, I. H., Lilley, M. D., Barriga, F. J. A. S., Baumberger, T., Flesland, K., Fonseca, R., Früh-Green, G. L., and Jorgensen, S. L. Discovery of a black smoker vent field and vent fauna at the Arctic Mid-Ocean Ridge. *Nature Communications*, 1(1), Nov. 2010. doi: 10.1038/ncomms1124.

Peterson, J. R. *Observations and modeling of seismic background noise*. 1993. doi: 10.3133/ofr93322.

Plaza-Faverola, A., Schlindwein, V., Pilot, M., Cooke, F., Sharma, R., Toh, F., Jensen, S., Kirk, H., and Pfeiffer, A. Ocean bottom seismics and acoustic surveys on fluid venting and seepage sites: West Barents Sea [dataset], 2026. https://hdl.handle.net/11250/5509581. Knipovich Ridge and Prins Karl Forland. Norwegian Research Information Repository (NVA).

Prothero, W. A. Ocean bottom seismometer technology. *Eos, Transactions American Geophysical Union*, 65(13):113–116, Mar. 1984. doi: 10.1029/eo065i013p00113.

Rau, G. H. and Hedges, J. I. Carbon-13 Depletion in a Hydrothermal Vent Mussel: Suggestion of a Chemosynthetic Food Source. *Science*, 203(4381):648–649, Feb. 1979. doi: 10.1126/science.203.4381.648.

Schlindwein, V. The Expedition PS137 of the Research Vessel POLARSTERN to the Arctic Ocean in 2023, 2023. doi: 10.57738/BZPM_0781_2023.

Schlindwein, V. and Schmid, F. Mid-ocean-ridge seismicity reveals extreme types of ocean lithosphere. *Nature*, 535(7611), 2016. doi: 10.1038/nature18277.

Schlindwein, V., Li, S., Kirk, H., and Schmidt-Aursch, M. C. Seismic soundscape of the Arctic Ocean: seasonal effects of sea ice and swell on deep-sea ocean bottom seismometer records. *Geophysical Journal International*, 242(1), Apr. 2025. doi: 10.1093/gji/ggaf143.

Schlindwein, V., Schmidt-Aursch, M., and Plaza-Faverola, A. Project Jøtul: DEPAS ocean-bottom seismometer operations at the Jøtul vent field, Knipovich Ridge. In *2023-2024. PANGAEA*. 2026. https://doi.pangaea.de/10.1594/PANGAEA.994133. dataset in review.

Schmidt-Aursch, M. C., Almendros, J., Geissler, W. H., Heit, B., and Yuan, X. Correction of nonlinear clock drift: the BRAVOSEIS Ocean-Bottom Seismometer Network in the Bransfield Strait, Antarctica. *Geophysical Journal International*, 245(1), Feb. 2026. doi: 10.1093/gji/ggag064.

Stachnik, J. C., Sheehan, A. F., Zietlow, D. W., Yang, Z., Collins, J., and Ferris, A. Determination of New Zealand Ocean Bottom Seismometer Orientation via Rayleigh-Wave Polarization. *Seismological Research Letters*, 83(4), 2012. doi: 10.1785/0220110128.

Sumy, D. F., Lodewyk, J. A., Woodward, R. L., and Evers, B. Ocean-Bottom Seismograph Performance during the Cascadia Initiative. *Seismological Research Letters*, 86(5):1238–1246, Aug. 2015. doi: 10.1785/0220150110.

Tian, J., Lin, J., Zhang, F., Xu, M., Zhang, Y., Guo, L., and Zeng, X. Time Correction of Ocean-Bottom Seismometers Using Improved Ambient Noise Cross Correlation of Multicomponents and Dual-Frequency Bands. *Seismological Research Letters*, 92 (3):2004–2014, Jan. 2021. doi: 10.1785/0220200358.

Vetter, E. W. and Smith, C. R. Insights into the ecological effects of deep ocean CO2 enrichment: The impacts of natural CO2 venting at Loihi seamount on deep sea scavengers. *Journal of Geophysical Research: Oceans*, 110(C9), 2005. doi: 10.1029/2004jc002617.

Webb, S. C. Broadband seismology and noise under the ocean. *Reviews of Geophysics*, 36(1):105–142, Feb. 1998. doi: 10.1029/97rg02287.

Wessel, P., Luis, J. F., Uieda, L., Scharroo, R., Wobbe, F., Smith, W. H. F., and Tian, D. The Generic Mapping Tools Version 6. *Geochemistry, Geophysics, Geosystems*, 20(11):5556–5564, Nov. 2019. doi: 10.1029/2019gc008515.

Zhang, H., Schmidt-Aursch, M. C., Geissler, W. H., and Xing, J. Characteristics of the Oceanic Ambient Seismic Noise Around Tristan da Cunha in the South Atlantic From OBS Data. *Journal of Geophysical Research: Solid Earth*, 128(6), May 2023. doi: 10.1029/2022jb025884.

Zhang, T., Li, J., Niu, X., Ding, W., Fang, Y., Lin, J., Wang, Y., Zha, C., Tan, P., Kong, F., Chen, J., Wei, X., Lu, J., Dyment, J., and Morgan, J. P. Highly variable magmatic accretion at the ultraslow-spreading Gakkel Ridge. *Nature*, 633(8028):109–113, Aug. 2024. doi: 10.1038/s41586-024-07831-0.